Journal of CO2 Utilization 67 (2023) 102303

Contents lists available at ScienceDirect

Journal of CO2 Utilization

journal homepage: www.elsevier.com/locate/jcou

Hybrid Bisphenol A non-isocyanate polyurethane composite with Mica powder: A new insulating material

Juliana J. Santos [a,*,1,2], José H. Lopes [a,b,3], Kelen M.F. Rossi de Aguiar [c], Mateus B. Simões [a], Jean-Claude MPeko [d], Renato G. Jasinevicius [e], Eder T. Cavalheiro [f], Hidetake Imasato [a], Ubirajara P. Rodrigues-Filho [a,*,1,2]

[a] São Carlos Institute of Chemistry, University of São Paulo (USP), Group of Chemistry of Hybrid and Inorganic Materials (GQMATHI), São Carlos, SP, Brazil
[b] São Carlos School of Engineering, University of São Paulo (USP), Materials Engineering Department, São Carlos, SP, Brazil
[c] Federal University of Technology – Parana (UTFPR), Group of Polymers and Nanostructures (GPaN), Toledo, PR, Brazil
[d] São Carlos Institute of Physics, University of São Paulo (USP), São Carlos, SP, Brazil
[e] São Carlos School of Engineering, University of São Paulo (USP), Mechanical Engineering Department, São Carlos, SP, Brazil
[f] São Carlos Institute of Chemistry, University of São Paulo (USP), Laboratory of Thermal Analysis, Electroanalytical and Solution Chemistry (LATEQS), São Carlos, SP, Brazil

ARTICLE INFO

Keywords:
Muscovite
Non-isocyanate polyurethane
Carbon dioxide
Insulation material
Bisphenol A

ABSTRACT

Non-isocyanate polyurethanes (NIPU) or hydroxyurethanes from CO_2 sourced monomers were prepared via a non-toxic route, which avoided the toxic isocyanate utilization with an excellent conversion ratio of cyclic carbonate, higher than 95%. The hybrid NIPU was prepared in the presence of aminosilylated-mica, used as reinforcement to improve mechanical properties, besides keeping the charge dissipation. The improvement of mechanical, thermal and electrical properties by silylated mica is attributed to higher crosslinking density in the organosilicate network. (attributed to the interfacial urethane linkage between the -NH_2 on the surface of the mica and the cyclocarbonates). It has been demonstrated the feasibility to produce candidate materials for replacing epoxy-mica paper hybrid system by an alternative CO_2 derived non-isocyanate hydroxyurethane-mica powder system. This system holds two advantages: CO_2 long-term capture and a more simplified hybrid formation, since no vacuum pressure impregnation (VPI) is necessary, does resulting on lower energy consumption.

1. Introduction

Dielectric materials for power applications such as spacers, cable terminations and machine insulation are exposed to high electric, thermal and mechanical stresses during operation. Due to the technical development towards higher electrical field strengths and frequently concomitant increased thermal loads, improved materials are required to meet those demands [1]. Improved insulating properties as well as high thermal conductivity are required for insulating materials for such applications. Composite and hybrid materials are the most used technological solutions for achieving the necessary requirements, being epoxy resin frequently applied for this purpose [2–6].

Epoxy resins are the most used polymeric material for insulating purposes since they combine interesting properties such as high mechanical strength and good thermal stability under the operational conditions of electrical equipment [4–7]. However, using raw epoxide system for insulating applications presents three main disadvantages: a) high exothermicity of the curing reactions, b) high brittleness due to high crosslinking density [8], c) very low thermal conductivity (0.2 W. mK^{-1}) [9]. Therefore, the addition of fillers has been used to overcome these drawbacks, especially those who improve the dielectric requirements. Among them, the phyllosilicates, such as Mica, are a material of choice as an epoxy filler due to its suitable cost-benefit [10].

Micas are layered materials which have a general formula $XY_{2-3}T_4O_{10}Z_2$ (X, Y and T being cations and Z anions). The most widely used type of mica for insulating purposes is the muscovite which presents the

* Corresponding authors.
E-mail addresses: julianajarussi@gmail.com (J.J. Santos), ubirajara@usp.br (U.P. Rodrigues-Filho).
[1] Av. João Dagnone, 1100, Jardim Santa Angelina, CEP 13563–120 - São Carlos – SP – Brazil.
[2] ORCID ID: https://orcid.org/0000–0002-1561–6524
[3] in memoriam.

https://doi.org/10.1016/j.jcou.2022.102303
Received 4 September 2022; Received in revised form 24 October 2022; Accepted 27 October 2022
Available online 10 November 2022

general formula $KAl_2(AlSi_3O_{10})(OH)_2$ [11]. Muskovite (from now on referred just as mica) has high thermal stability and high dielectric strength at 20 °C (60–70 kV/mm), high electrical resistivity, large bandgap (10.50 eV) and low dielectric loss factor (3.10^{-4}) [12]. Mica paper is the most common shape of mica for insulating cables and electrical machines for several decades [13,14] due to its good dielectric properties and the corona resistance. Aside mica paper/epoxy being the most common insulating composite, other systems have been also used, for instance, the aromatic polyamide/mica paper composite named MICAFOLD® [15,16].

Many approaches have been used to improve the toughness of epoxy resins such as introducing either polysesquisiloxanes [17], or carboxy terminated butadiene acrylonitrile copolymers (CTBNs) [18], or isocyanate-modified rubbers [19], or blocked isocyanates [20] or polyurethanes [21].

Polyurethanes (PUs) are a widespread class of polymeric materials having many different aspects compared to other polymers. In addition, PU retains its elasticity and strength over a long range of conditions and even very rigid PUs can be stretched to substantial elongations and will still return to their original dimensions. Because of this and other features, PUs are nowadays used in applications present in everyday life, such as furnishing, cars, clothing, shoes, elastomers, coatings, wall and roofing insulation as well as on biomedical applications [22–26]. Conventional PUs are synthesized by reacting a polyol and a polyisocyanate [26]. The grafting of isocyanate reactive groups on hydroxyl groups present in epoxy resins results on an epoxy-PU material. Aiming a coating as a film, improving materials´ toughness demands a highly anhydrous environment to prevent the formation of urea and release of CO_2, once for insulation purposes, the presence of bubble or microbubbles caused by the CO_2 formation is a drawback, as well as the moisture, forasmuch it leads to a lower electrical performance of the insulation material. Furthermore, isocyanates present high toxicity, carcinogenicity and ecotoxicity [27,28], therefore, more sustainable routes for poly(urethane)s without using isocyanate have been used, thus resulting on a new class of PUs named non-isocyanate polyurethanes (NIPU) [29–31]. These NIPUs may be synthesized through polycondensation, rearrangement, ring-opening-polymerization or polyaddition [32–37]. The ring-opening polymerization by the aminolysis of cyclocarbonates produces poly(hydroxyurethanes), which have additional hydroxyl groups vicinal to the urethane bond. Those β-hydroxyl groups form inter- and intramolecular hydrogen bonds which in turn result on a hydrolytic resistance and moisture insensitive [38] compared to conventional polyurethane system; plus, the ability to blend with hydrophilic biopolymers, as it can be seen by its compatibility with starch reported by Ghasemlou et al. [39].

The preparation of hybrid epoxy-NIPU has been recently successfully achieved by Lambeth et al. [40], Cailol et al. [41] as well as by Bouhendi et al. [42]. The materials showed a decrease in the rubbery modulus (Ér) of the epoxy/NIPU hybrids as compared to the pristine epoxy samples which has been assigned to a decrease in crosslink density, thus, confirming the use of NIPU in these hybrid systems as a possible pathway for toughness improvement in these insulating composites.

Compatibilization of inorganic fillers such as mica with organic resins has been achieved by silylation chemistry using different alkoxysilanes [43–49]. The addition of amino silylated mica strongly influences the miscibility of multiphase composites as well as results on a slight reduction in the cold-crystallization temperature and crystallinity of the composites, as observed by differential scanning calorimetry (DSC) reported by Jia et all [50].

In this report, we aim to employ a system which is attractive not only due to the total or partial replacement of the traditional epoxy/mica paper system by a NIPU bearing hybrid but also replacing the mica paper by silylated mica powder. The partial or total replacement of the epoxy resin allows materials´ toughness improvement as well as brings the opportunity to use this new insulating material as a CO_2 sink. Therefore, this material collaborates for the sustainability of CO_2 capture, storage and use processes once the gas used as raw material is collected from geological storage sites or from industrial sites [51–55]. On the other hand, the replacement of mica paper by mica powder may considerably simplify the production process since no vacuum is needed, such as used in the vacuum pressure impregnation (VPI) process, or manual wrapping of prepags around the copper conductors such as in the resin rich (RR) technology [12]. To gain some insight on the size of the mica paper market a recent business report estimated the global mica paper market to be as large as US$ 50 million in 2024 [56] with China being the largest producer with 48 kMT by 2015. Finally, but not least the use of silylated mica powder is introduced to improve the compatibility and strength of the interface between the inorganic and organic components [57,58].

2. Experimental

2.1. Materials

The epoxy used was EPON 828 Bisphenol-A Diglycidyl ether, DGEBA, (M_n = 380 $g.mol^{-1}$ and equivalent epoxy weight between 185 and 192 $g.eq^{-1}$) supplied by Hexion Indústria e Comércio de Epoxi Ltda, Brazil. The micaś powder used was the pristine muscovite and, the 1% silylated Muscovite Mica, prepared by treating with 3-aminopropyltriethoxysilane (APTES) kindly supplied by IMERYS Itatex, Brazil. Tetraethylammonium bromide (TEBA) 99%, Isophorone diamine (IPDA) 99% 1,8-Diazabicyclo [5.4.0] undec-7ene 98% (DBU), 2-ethoxyethanol 99% were purchased from Sigma Aldrich. Zinc Chloride (II) ($ZnCl_2$) 98% was purchased from Merck, Germany. Carbon Dioxide (CO_2) 99.99%, was purchased from Linde Gas Brazil. Acetone 99.9%, 1-Methyl-2-pyrillidone 99% and Tetrahydrofuran (THF) were purchased from VETEC, Brazil. All materials were used as received without further purification.

2.2. Synthesis

2.2.1. Production of Cyclocarbonate of Bisphenol A (CCGEBA)

Optimized CO_2 cycloaddition to DGEBA to obtain the CCGEBA was performed according to Scheme 1. Briefly, 20 g of DGEBA dissolved in 15 mL of 2-ethoxyethanol and 10 mL of methylvinyl pyrrolidone was transferred into a high-pressure reactor Parr Model 2192HC4 (stainless steel T316SS). Then, the homogeneous catalysts tetraethyl ammonium bromide (TEBA) and anhydrous $ZnCl_2$ were slowly added under stirring (200 rpm) until complete dissolution. The catalysts and co-catalyst amount were 1.0 wt% and 0.1 wt%, respectively. The reactor was closed and purged with CO_2 for 5 min before being pressurized with 100 psi (6.80 atm) of CO_2. The reaction temperature was set to 120 °C under a stirring rate set to 200 rpm for 24 h. After synthesis, the reactor was allowed to cool down and the excess of CO_2 was released. Afterwards,

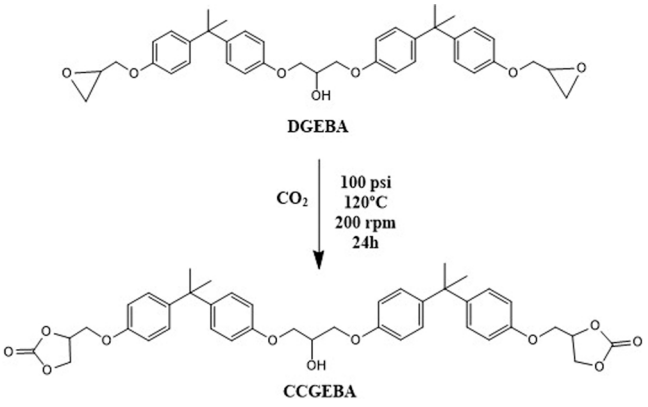

Scheme 1. Schematic representation of the synthesis of CCGEBA by CO_2 cycloaddition into DGEBA.

the catalysts were removed from the obtained material via solvent extraction (water-ethyl acetate 1:3) and the solvent removed by rotoevaporation. The CCGEBA obtained was a yellow liquid. It is valid to point out that no reaction between the 2-ethoxyethanol and DGEBA was observed under the reaction conditions.

2.2.2. Synthesis of NIPU

CCGEBA (10.3 and 11.4 mmol according to Table 1) was dissolved in 7 mL of acetone at 35 °C for 1 h in a 20 mL borosilicate glass flask. After complete solubilization the IPDA (9.4 and 7.0 mmol according to Table 1), DBU (0.1 wt%) was added and the solution was kept under constant mixing at 60 °C for 1 h under reflux (Scheme 2). Afterwards, the muscovite (silylated or not) was added (40 wt%) and magnetically stirred for 1 h at 60 °C. Thus, most of the solvents was evaporated in an oven at 90 °C for 1 h under vacuum, 11 mmHg. Finally, the hydroxyurethane is poured into a Teflon mold and kept for 24 h at room temperature and another 24 h at 75 °C in a conventional oven, obtaining a solid thick film. Table 1 describes all formulations used to obtain the hybrids in this study alongside their abbreviations.

2.3. Characterization methods

2.3.1. Epoxy equivalent determination

The epoxy equivalent of the resins (E) was obtained by volumetric titration according to ISO 3001–1999 [59] in order to quantify the yield of conversion of epoxy into cyclocarbonate, by the quantitative determination of the percent epoxide content. Briefly, a sample of CCGEBA was dissolved in dichloromethane and to the resulting solution performed an indirect titration utilizing standard Perchloric acid 0.1 N (previously standardized with Bisphenol-A Diglycidyl ether) in the presence of an excess of Tetraethylammonium Bromide and Crystal Violet indicator solution 0.1 wt%. Hydrogen bromide generated in situ by the addition of perchloric acid to the quaternary ammonium halide rapidly opens the oxirane ring. The yield of the conversion is calculated by the EEW, epoxy equivalent weight (Eq. (1)), of the DGEBA and CCGEBA, where 43 is the molar weight of the epoxy ring and E is the weight percent epoxide, as follows in the Eq. (2).

$$EEW = \frac{43 \times 100}{E} \tag{1}$$

$$E = \frac{4,3 \times V \times N}{W} \tag{2}$$

Where, E : weight percent epoxide, V : titration volume (mL) and N : real normality of perchloric acid solution.

2.3.2. Elemental analysis

Elemental analysis of carbon, hydrogen and nitrogen were performed in a 2400 Series II CHNS/O Elemental Analyzer (Perkin-Elmer). The elements were quantified by the Pregl-Dumas method, in which the samples are subjected to combustion under oxygen atmosphere and the released gases are detected in a thermal conductivity detector (TCD).

Table 1
Hybrid formulations and its abbreviations.

Sample code	CCGEBA (mmol)	IPDA (mmol)	CCGEBA: IPDA (molar ratio)	Mica (muscovite) (wt%)[a]	Silylated mica (wt%)[a]
NIPU1	10.3	9.4	1.1	0	0
NIPU:M1	10.3	9.4	1.1	40	0
NIPU: Ms1	10.3	9.4	1.1	0	40
NIPU: Ms2	11.4	7.0	1.6	0	40

The DBU (catalyst) weight percentage is relative to the total weight of the formulation, including solvent and it was kept at 0,1% (wt) for all formulations.
[a]The weight percentages are relative to the dry mass of the solid.

2.3.3. X-ray photoelectron spectroscopy (XPS)

Pristine and silylated muscovite were characterized by X-ray photoelectron spectroscopy in a Physical Electronics Versa Probe 5000™ spectrometer. The spot size analyzed at the sample was ≈ 500 μm x 1500 μm and the take-off angle was (45° ± 20). Monochromatic AlKα X-ray (1486.6 eV) at 85 W was used to promote sample photoemission. The charge correction was made using Low energy electron flood-gun, no ion sputtering was used. The base pressure at the analysis chamber was ~5×10^{-8} Torr.

2.3.4. Solid state nuclear magnetic resonance

Solid state nuclear magnetic resonance spectra recorded at Avance III HD spectrometer, magnetic field of 9.4 T (Bruker, USA) at 4 mm o.d. zirconia rotor, external adamantane CH_2 reference for ^{13}C delta reference (38.48 ppm from tetramethylsilane) and for ^{29}Si an external reference of the sodium trimethylsilylpropanesulfonate. Standard ^{13}C NMR CPMAS at 10 kHz magic angle spinning. ^{1}H P90 of 3.8 μs, Hartmann-Hahn cross polarization ^{1}H to ^{13}C during 4.5 s of contact time, ^{13}C acquisition time of 41 ms with heteronuclear decoupling, sweep width of 502 ppm, Time domain sampling 4096, recycle time of 5,0 s, NS 4096. ^{13}C Spectral editing CPPI experiment. Standard CPMAS sequence combined with polarization inversion time of 80 μs before acquisition to obtain positives nonprotonated carbon and CH_3, negatives CH_2, and practically null CH signals. ^{13}C Spectral editing CPNQS experiment. Standard CPMAS implemented with two pulses of 150 μs having an 8.2 μs inversion pulse on ^{13}C channel between them for dephasing the ^{13}C spins coupled to ^{1}H before heteronuclear ^{13}C free induction decay recording to suppress non-quaternary carbon. ^{29}Si NMR MAS at 10 kHz magic angle spinning. High power ^{1}H decoupling pulse sequence, 4 μs excitation pulse, TD 2048, NS 1024, SW 299.6451 ppm, acquisition time 0.0430 s, recycling delay time 10 s. All the NMR experiments were graciously performed at Embrapa Instrumentaç ão.

2.3.5. Water absorption

The water absorption by the samples was performed according to ASTM D570–98 [60]. In brief, plates of 20 × 20 x 2 mm were cut, always in triplicates. These dried specimens were weighed, then left for 24 h immersed in a beaker with distilled water at room temperature (25 °C). Afterwards, the samples were removed and dried on absorbent paper towels and reweighed. The water absorption content was calculated according to Eq. (3):

$$Water\ Absorption\ (\%) = \frac{weight_{wet\ sample} - weight_{dry\ sample}}{weight_{dry\ sample}} \times 100 \tag{3}$$

2.3.6. Swelling index and gel content

Swelling Index and gel content were obtained according to Cornille et al. [41].

Swelling index: three samples (30 mg each) were separately put into 30 mL THF for 24 h. The swelling index, SI, is given by Eq. (4), where m_0 is initial mass and m_1 is mass after swelling in solvent.

$$SI = \frac{m_1 - m_0}{m_0} \times 100 \tag{4}$$

Gel content: After SI measurement, the three tabs are dried in a ventilated oven at 50 °C during 24 h. The gel content GC is given by following Eq. (5), where m_0 is initial mass and m_2 is mass after drying.

$$GC = \frac{m_2}{m_0} \times 100 \tag{5}$$

2.3.7. Static water contact angle (wetting) analysis

The static water contact angles were measured using an ATTENSION Tensiometer. The drop volume was kept constant at 3 μL for each

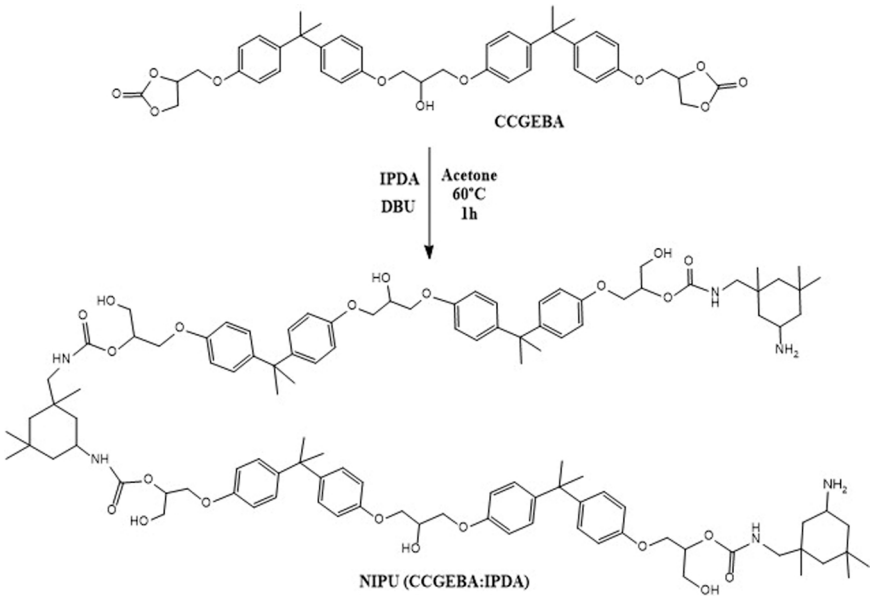

Scheme 2. Schematic representation of the ring-opening by aminolysis of cyclocarbonates of CCGEBA with IPDA.

measurement and the final value of the contact angle was the mean of three measurements at three different regions of the sample. The images were acquired on a CCD camera and the images analyzed with the SCAN 20 Data Physics software, 6 images / second, lasting 10 s each image. Ultra-pure water was used all through the experiment. Software calibration was done with a tungsten ball with a diameter of 3.9999 mm.

2.3.8. Dieletric response

2.3.8.1. Impedance spectroscopy. Impedance spectroscopy measurements were carried out at São Carlos Institute of Physics using a frequency response analyzer Solartron 1260 A Impedance Analyzer. Data acquisition was carried out with the SMaRT Impedance Measurement Software. The experiments were made using a two-electrode configuration in the frequency range from 0.1 kHz to 100 kHz. The applied voltage amplitude was 300 mV. The 0.19 g samples were cut in a disc-shape format with 10.6 mm diameter, 1.83 mm thick. The sample surfaces were painted with silver and carbon conductive adhesive to promote contact with the electrodes, respectively for NIPU:M1, NIPU:Ms1 and NIPU:Ms2 samples. The measurements were obtained at room temperature (25 ºC) as well as at 50 °C. The imaginary (C) and real part (C) of the complex capacitance (C) are described in Eqs. (6) and (7).

$$C(\omega) = C'(\omega) - iC'\prime(\omega) \tag{6}$$

$$C'(\omega) = \frac{\varepsilon_0 \varepsilon A}{d} \tag{7}$$

Where: Ɛ: Dielectric Constant or Dielectric Permissibility, $Ɛ_0$: Vacuum permittivity (8.854×10^{-12} F.m^{-1}), A: Area of the electrodes, d: Samplés thickness (distance between the electrodes).

From the imaginary and real capacitance, it is possible to calculate the dielectric constant (ε) as well as the loss factor (tgδ) as follows in Eqs. (8) and (9).

$$\varepsilon = \frac{C'd}{\varepsilon_0 A} \tag{8}$$

$$tg\delta = \frac{C'\prime}{C'} \tag{9}$$

2.3.8.2. Dielectric strength. On the one hand, high voltage tests called dielectric breakdown or strength tests were performed at room temperature (25 °C) to appraise the maximum electrical strength of these materials as insulators. These measurements were graciously performed at 3 M Brazil. Accordingly, the materials are stressed with an increasing high AC or DC voltage until reaching the non-linear region of current, towards which data of breakdown or perforation happening are collected. The data were obtained according to ASTM standard: D 149–20 [61], using a TFI-30 equipment (Triel Ltda, Brazil) and the short-time test protocol as voltage application methodology. The rate-of-rise all through the experiments was 500 V.s^{-1}, and the time to failure was between 20 and 40 s. The dielectric strength was calculated according to Eq. (10).

$$Dielectric\ Strength = \frac{Disruptive\ Tension}{Sample\ Thickness} \tag{10}$$

The thickness of the specimens ranged between 0.4 and 0.9 nm. For each material, three independent measurements were performed on plate-like samples cut from the same sample.

2.3.9. Thermogravimetric analysis

The thermogravimetric analysis (TGA) was carried out using Shimadzu's TGA 50 according to Yee and Stephens [62]. Briefly, square shape samples (2.5 ×2.5 mm) were submitted to a temperature scanning range from 25 ° to 800 °C (scan rate of 20 °C.min^{-1}) under a nitrogen atmosphere and flow set to 50 L.min^{-1}. All the reported temperatures are onset values. The thermogravimetric analysis (TGA) under synthetic air was carried out using a SDT-Q600 Simultaneous TGA / DTA (TA Instruments, USA), the heating rate was 10 °C.min^{-1} between 23 and 1000 °C under dry synthetic air and flow set to 50 mL.min^{-1}. All the reported temperatures refer to onset values.

2.3.10. Nanoindentation

Based on the Oliver–Pharr model [63] the nanohardness (H) measurements were carried out on the samples using a commercial nanoindentation machine (Nanovea PB 100, Irvine, CA). The depth and force sensing resolutions of the machine were 0.003 nm and 0.028 μN, respectively. The machine was calibrated with nanoindentation based independent evaluation of nanohardness (8.9 GPa) of a fused silica. The experiments were conducted at five different locations, 15 μm apart, with an applied load of 30 mN using a Berkovich indenter. All te measurements were performed at Escola de Engenharia de São Carlos, Universidade de São Paulo.

2.3.11. Vibrational spectroscopy

The attenuated total reflectance (ATR) Fourier Transform Mid-Infrared (FTIR) spectra were collected using a Tensor 27 spectrometer (Bruker Optics, Germany) coupled to an IRIS ATR accessory (Pike Technologies, USA) equipped with Ge crystal. The spectral resolution was 2 cm^{-1} using 64 scans.

2.3.12. Optical profilometry

Optical profilometry with a WYKO NT1100 noncontact optical profiler (Bruker, Tucson, AZ) was employed to measure the surface textures and structures of the stratum corneum on the millimeter lateral scale. Vertical scanning interferometry mode (VSI) was used since this is suitable for detecting height differences of up to 1 mm [64]. All optical profilometry images were measured in air (ca. 30% r.h.) at room temperature. The roughness parameters collected were average roughness (R_a), root mean square roughness (R_q), skewness (S_{sk}) and kurtosis (S_{ku}) [65]. All the measurements were done at the Mechanical Engineering Department of the Engineering School at São Carlos, University of São Paulo (USP).

2.3.13. Scanning Electron Microscopy (SEM)

The fractographies of the hybrids were obtained in a ZEISS LEO 440 (Cambridge, England) coupled with an OXFORD detector, model 7060, operating at 15 kV, 2,82 A and working distance of 25 mm. All samples were coated with thin gold film by a Coating System BAL-TEC MED 020 (Baltec, Liechtenstein) utilizing the parameters: pressure of 0,02 mbar, current of 60 mA and deposition rate of 0,60 $nm.s^{-1}$.

3. Results and discussion

3.1. CCGEBA characterization

The cycloaddition of CO_2 into DGEBA, which reaction scheme is presented in Scheme 1, can be confirmed in the infrared spectra in Fig. 1, by the disappearance of the peak related to the epoxy asymmetric vibration (950 cm^{-1}) and the appearance of the peak corresponded to the carboxyl of cyclocarbonate (υ_O(C═O)O) at 1800 cm^{-1}.

Fig. S1 shows the ^{1}H NMR spectrum of CCGEBA and the characteristics signals of hydrogens were: carbonate ring ($\delta = 4.51$ ppm and $\delta = 5.05$ ppm) and some unreacted epoxy groups ($\delta = 3.3$ ppm). The correlation between the integrated area of the carbonate ring and epoxy group peaks in the ^{1}H NMR spectrum was used to estimate the reaction yield. It turns out the yield of the epoxide conversion into cyclocarbonate was estimated as 94.5% in opposition to 97% obtained by epoxide titration.

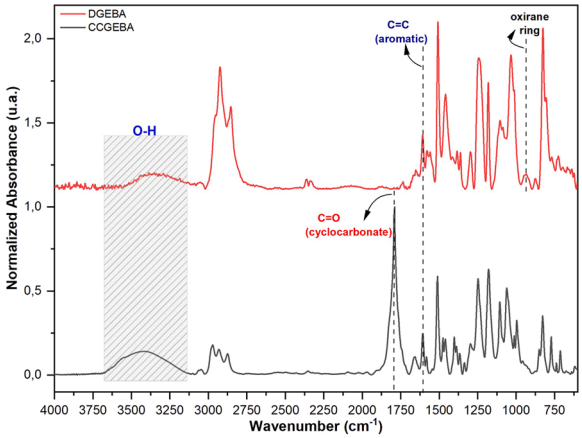

Fig. 1. ATR-FTIR of DGEBA (red) and CCGEBA (black).

3.2. Characterization of NIPU polymer

The NIPU was obtained by the aminolysis of CCGEBA with IPDA, as represented by the reaction in Scheme 2. The reaction was followed by FTIR spectroscopy (Fig. 2). In particular, the hydroxyurethane formation can be monitored by the changes of the carboxyl absorption. The initial CCGEBA carboxyl stretching absorption identified at around 1800 cm^{-1} (from cyclocarbonate) is shifted to 1702 cm^{-1} (urethane C═O) and a new band at 1541 cm^{-1} was observed after successful reaction of CCGEBA and –NH_2 groups of IPDA. This peak is related to the stretching of the N-H bond from the urethane linkage [33,66].

It is important to notice that no peak regarding the presence of cyclocarbonate was observed in the NIPU spectrum, thus characterizing a fully cyclocarbonate conversion into hydroxyurethanes.

In the insert in Fig. 2, the broad peak between 1680 and 1730 cm^{-1} can be assigned to amide I, while the region between 1530 and 1560 cm^{-1} can be assigned to amide II and those from 1430 to 1460 cm^{-1} are tentatively assigned to amide III [66].

3.3. Characterization of silylated mica

The wide scan X-ray photoelectron spectra of the pristine and silylated muscovite are presented in Supplementary Section (Fig. S2). The weak N1s photoemission peak on the surface of the silylated muscovite is proof of the silylation by APTES [44,67]. The nitrogen and carbon atomic percentages obtained from XPS are 2.6% and 11%, respectively. The nitrogen and carbon bulk were measured by traditional elemental analysis of the silylated mica, showing 0.22% and 0.26%, respectively. The nitrogen content for the pristine mica was 0.06%. Overall, these results confirm the surface modification by APTES on the muscovite mica surface.

3.4. Solid state nuclear magnetic resonance

^{29}Si Cross-Polarization (CP) *Magic Angle Spinning* (MAS) Nuclear Magnetic Resonance (NMR) was used to characterize the muscovite dispersed into the hydroxyurethanes.

The 4 ms cross polarization contact time CPMAS results (Fig. S3) in a single signal at 95.0 ppm. Both HPDec (high-power decoupling) spectra appear to exhibit three partially resolved resonances in the range −75 ppm to −92 ppm and a fourth under the unique high signal observed in the CPMAS spectrum. Besides, as effect of increasing the recycle delay from 10 s to 100 s, a peak at 107 ppm is risen.

Marsmann [68] on silicate solutions ^{29}Si NMR studies has assigned the −107.2 ppm signal to the internal silicon, Si (–OSi–)$_4$, of branching groups, while a signal at −94.6 ppm to intermediary silicon in the chain branching groups, respectively, Q_4 and Q_3 according to the silicate nomenclature. The kinetics of cross polarization depends on the constant time of raising due to spin locking pulse on sensitive nucleus, generally ^{1}H, during contact time reaching the Hartmann-Hann conditions. In the present research, the time constant should be T_{HSi}, it means, cross polarization from ^{1}H to ^{29}Si. It is possible to realize that if there is no ^{1}H in proximity to the, for instance ^{29}Si, the mechanism does not operate. At same time the spin-lattice relaxation in the rotating frame takes place, $T_{1\rho}$, should be shorter according to the abundance of sensitive nucleus [69]. By the presence of a unique signal at −95.0 ppm in the 4 ms CPMAS there is only Q_3 group sensitive to the cross-polarization and the Q_4 is expected to be insensitive due to the absence of hydrogen in the wet muscovite. The raising of Q_4 signal at 107.3 ppm upon increase to recycle delay in the HPDP experiments should be explained by very long relaxation time even the more rigid structure [70,71].

The fitting by gaussian peak of CPMAS spectrum (Figs. S4 and S5) result in a thick peak at −95.0 ppm (74 Hz). Therefore, it was assumed previously in the one pulse HPDec 100 s spectrum fitting, including beyond three gaussians a fourth one due to large feature under −95 ppm peak and additional gaussian at −107 ppm for Q_4 silicate. The fitting

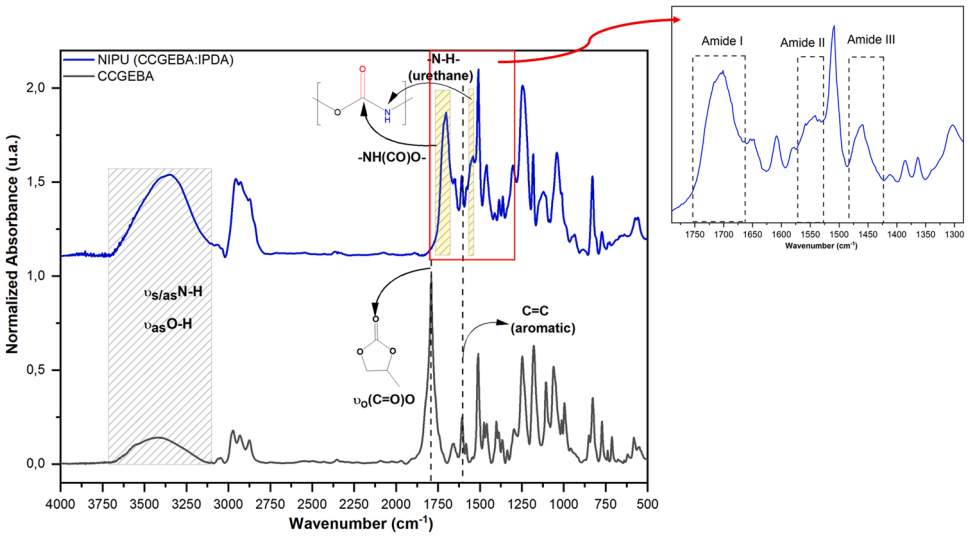

Fig. 2. FTIR spectra of the CCGEBA (black line) and its respective NIPU (blue line), the arrows point out the most important characteristic feature of the cyclocarbonate and urethane bonds. The insert emphasizes the amide vibrations.

resulted in the two narrow gaussians at −107.3 ppm (44 Hz) and at −95.0 ppm (61 Hz instead of 74 Hz) and four broad gaussians at −83.2 ppm (313 Hz), −86.0 ppm (175 Hz), –89.2 (406 Hz), and −95.0 ppm (201 Hz).

The muscovite belongs to the 2:1 phyllosilicate tightly condensed layer built by a central aluminum dioctahedral sheet sharing the edge and two aluminosilicate tetrahedral sheets sharing the vertices, one above and another bellow. Both sheets correspond to the hexagonal honeycomb pattern. In the tetrahedra sheet the apical oxygens pointing to the same direction which coordinate the Al^{3+} of dioctahedral $Al_4(OH)_{12}$ sheet to form the individual 2:1 phyllosilicate layer. The aleatory isomorphous substitutions of Si^{4+} for Al^{3+} (3Si:1Al) in the tetrahedral sheets result the negative net charge. The neutrality of crystal can be restored by presence of cation ions as K^+ in the inter 2:1 phyllosilicate layer space. Then the muscovite unitary cell presents $K_2Al_4(OH)_4(AlSi_3O_{10})_2$ composition [72].

Since the Lippmaa and colleagues earliest report [73], the ^{29} Si NMR has been applied for specifying the aluminosilicates silicon sheet sites taken the advantage of additional paramagnetic and dioctahedral distortion effects on the chemical shift proportional to the tetrahedra silicon, SiO_4, substitution by tetrahedra aluminum, AlO_4. These frameworks define the Q^3 Si environments in the tetrahedral planes. According to the successive isomorphous substitutions they would create Q^3(0Al), Q^3(1Al), Q^3(2Al), and Q^3(3Al), sites [73,74]. In the case of muscovite, they are expected to observe mainly three ^{29}Si NMR signals. The −83.2 ppm, −86.0 ppm, and −89.2 ppm could be assigned to Q^3(2 Al), Q^3(1 Al), and Q^3(0 Al), respectively [75,76].

For the 2:1 phyllosilicate that are in accordance of Loewenstein's rule, i. e., in the tetrahedral framework there is no Al–O–Al linkages when require the coordination higher than four [76], it can be evaluated the Si/Al ratios by Sanz and Serratosa, in Eq. (11), from which it can be evaluated the fraction of AlO_4 tetrahedra, X_{Al} [75]:

$$\frac{Si}{Al} = \frac{\sum_{n=0}^{3} I_n}{\frac{1}{3}\sum_{n=0}^{3} nI_n} \tag{11}$$

From the Gaussian fitting data result the Si:Al 3.7 instead of 3. One reason should be the presence of some sedimentary impurities like smectite or illite, which can either explain the wide signal at −95.0 ppm. The smectite is characterized by ^{29}Si NMR signal of −89.5 ppm, Q^3(1Al), and –94.2, Q^3(0Al), meanwhile, −83.0 ppm, −86.5 ppm, and −89.5 ppm signals can be assigned to illite's Q^3(2Al), Q^3(1Al), and Q^3(0Al), respectively [76].

The ^{29}Si NMR spectroscopic pattern of muscovite can be observed in the spectra of both NIPU hybrids (Fig. 3), indicating that the synthesis procedures did not alter the mica structure.

3.5. Water absorption of the prototypes

Water absorption is a key parameter for insulating hybrid materials. Indeed, water absorption by the insulation system of the generator stator yields an insulation resistance drops by almost two decades from normal conditions. Furthermore, once wet the insulation bar has a much higher temperature dependence compared to a dry bar [71]. Table 2 shows the water absorption capacity for the samples. Higher water absorption capacity is achieved by using non-silylated mica filler, NIPU:M1, instead of silylated mica, NIPU:Ms1. Indeed, NIPU:Ms1 surprisingly has a very similar water capacity than NIPU1. Increasing cyclocarbonate:IPDA molar ratio (NIPU:Ms2) resulted in more than ninefold the water absorption capacity than NIPU:Ms1, due to a higher porosity of the hybrid, as better discussed in the Gel Content Section 3.6.

3.6. Swelling index and gel content

The polymer and composites swelling in tetrahydrofuran is an indirect approach to measure the crosslinking degree as well as gel content.

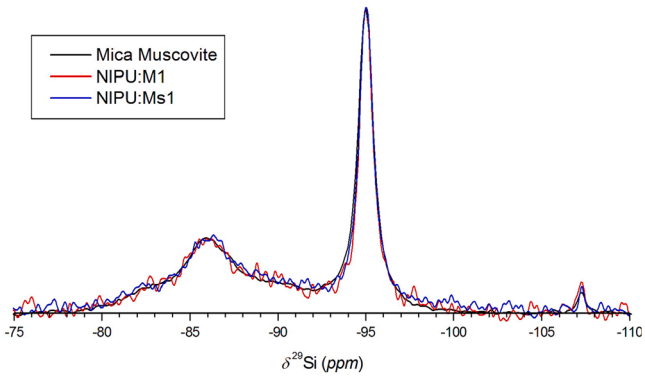

Fig. 3. ^{29}Si 79.46 MHz HPDec, recycle delay 100 s, pulse 3.8 μs, spinal64 acquisition proton decoupling Pristine Mica muscovite (black line) hybrid NIPU:M1 (red line) and NIPU:Ms1 (blue line).

Table 2
Water absorption capacity according ASTM D 570 for pristine NIPU1 and its hybrids.

Prototype	Water absorption (%)
NIPU1	2.48
NIPU:Ms1	2.11
NIPU:Ms2	19.00
NIPU:M1	9.56

Table 3
Swelling Index (SI) and Gel Content (%).

Prototype	Swelling index (%)	Gel Content (%)
NIPU1	Dissolved*	Dissolved*
NIPU:Ms1	93	23
NIPU:Ms2	Dissolved	Dissolved
NIPU:M1	Dissolved	Dissolved

* in THF.

Table 3 summarizes the swelling index (SI) and gel content (GC) obtained for all the materials. The organic matter for all but the NIPU:Ms1 has been completely dissolved by THF, thus reinforcing the water absorption inference in regard to the higher crosslinking degree for this silylated mica hybrid. This crosslinking density is referred to the interfacial urethane linkage between the -NH_2 on the surface of the mica and the cyclocarbonates. As mentioned in Water absorption Section 3.5, the NIPU:Ms2 hybrid has a higher CCGEBA:IPDA ratio resulting in less cyclocarbonate available to react with silylated mica, therefore yielding a lower crosslinking density. In addition, through the analysis of SEM of the hybrids (Fig. S6), it was not possible to observe in the fractographies, obtained under liquid nitrogen, of NIPU:Ms1 (Fig. S6-A) and NIPU:Ms2 (Fig. S6-B) any morphological differences.

3.7. Surface roughness and water wettability

The surface morphology of the NIPU:M1 sample is shown in Fig. S7. The insert photography in Fig. S7-A displays a crackled surface probably due to muscovite segregation and formation of large shatters, as shown in Fig. S7-B. Fig. S7-D shows the image of a single "shatter" with a very smooth surface as compared to Fig. S7-B, which can be inferred by the much smaller depth scale at the right side of these figures. Fig. S7-C shows the brownish region in the Fig. S7-B which was tentatively assigned to a hydroxyurethane rich region. The average roughness (R_a) and root mean square roughness (R_q) of the NIPU:M1 muscovite region is higher than the NIPU:M1 hydroxyurethane region, 3.08 and 3.93 μm versus 1.64 and 1.22 μm, respectively. Their negative skewness (S_{sk}), between − 0.41 and − 1.45, indicates a surface roughness dominated by steep valleys, with larger height asymmetry displayed by the NIPU:M1 hydroxyurethane region [65]. The kurtosis (S_{ku}) describes the sharpness of the probability density of the height profile, the NIPU:M1 presented S_{ku} between 3.47 and 6.07. Therefore, $S_{ku} > 3$ indicates leptokurtoic distribution, and thus the morphology is composed of relatively many high peaks and low valleys. Both regions have R_{ku} higher than 3 with NIPU:M1 hydroxyurethane region standing 5.95 versus 4.03 for the NIPU:M1 muscovite rich region.

The NIPU:Ms1 and NIPU:Ms2 are more homogeneous samples, thus, their R_a values are 1.92 ± 0.78 and 1.46 ± 0.62 μm, respectively, and R_q values 3.10 ± 1.83 and 1.62 ± 1.42 μm. It turns out the use of silylated mica as reinforcement filler instead of pristine results on more homogeneous surface.

3.8. Vibrational spectroscopy

The ATR-FTIR spectra of the NIPU, NIPU:M1 and NIPU:Ms1 are shown in Fig. 4. The Amide I, II and III bands are related to the peaks in the region from 1460 to 1730 cm^{-1}, as better discriminated in Section 3.2. All the spectra are very similar except by the region between 900 and 1080 cm^{-1}, gray rectangle, that shows broader convoluted peaks for the NIPU:M1 hybrid.

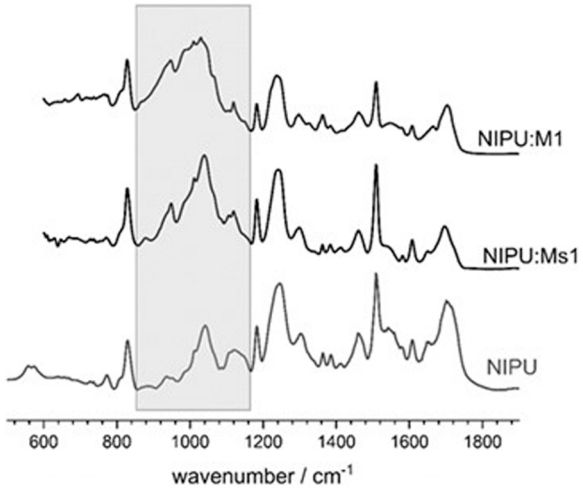

Fig. 4. ATR-FTIR of the NIPU, NIPU:M1 and NIPU:Ms1.

3.9. Solid-state ^{13}C nuclear magnetic resonance

For the muscovite CPMAS ^{13}C NMR spectrum no signal is observed (Fig. 5-A). However, they were obtained distinct spectra for the NIPU:M1 and NIPU:Ms1. Aiding the interpretation, the Gaussian fitting of spectra was performed (red lines). The second derivative of spectra provided the initial hints for the positions of the gaussians (not shown). The chemical shifts (δ ^{13}C, ppm), the line width (W, Hz), and the relative areas assuming the signal at 144.0 ppm to two carbons per one fragment of bisphenol A (which explanation will be discussed afterwards) [77], were collected in the tables splitting the spectra in two zones, from 170 ppm to 100 ppm, and between 90 ppm and 10 ppm.

Aiming to identify the chemical structure of carbons overlapped with CPMAS experiment, the CPPI and CPNQS editing sequences were applied, Figs. S8 and S9. The standard CPMAS protocol associated to the selective polarization inversion time (CPPI) is useful to differentiate the group of carbons, which calibration to 80 μs gave practically null signal for CH, negative signal for CH_2, and positive ones for C and CH_3 [78]. Otherwise, ^{1}H-^{13}C dephasing standing out mainly the weakly coupled carbon to the hydrogen dipole, like free rotating methyl groups [79] and the stated in the general sense the quaternary carbons [80], both as positive signals, and mainly suppressing others with residual CH signals

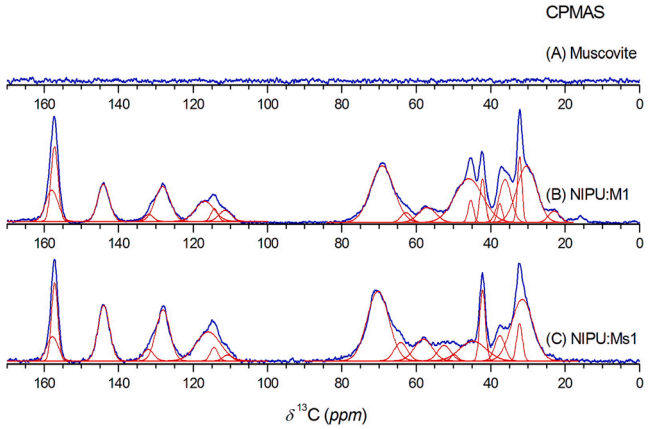

Fig. 5. ^{13}C NMR CPMAS. (A) mica muscovite; (B) NIPU:M1; (C) NIPU:Ms1.

(CPNQS). Based on these set of CP experiments, the main groups of carbon types were identified.

Based on the literature assignment [77], the ^{13}C NMR signals region from 170 ppm to 100 ppm could be useful to prove the integrity of bisphenol A biradical moiety, O–Ph–C(CH_3)$_2$–Ph–O. Considering one mol of bisphenol A moiety, the 157 ppm band can be resolved into two Gaussians. One at 157.2 ppm for NIPU:M1 and NIPU:Ms1 (2 carbons per mol of bisphenol A fragment) that can be assigned to the quaternary aromatic carbon of phenyl (Ph–O) end, and another at 157.9 ppm (2 carbons) for NIPU:M1 sample and 157.8 ppm (1 carbon) for NIPU:Ms1. Ochiai and cols [77]. reported that the amide carbonyl and this aromatic carbon are practically superimposed. The signal at 144.0 ppm (2 carbons) for both hybrids can be assigned to the quaternary carbon of opposite side of Ph. The ortho carbon relative to the phenyl oxygen CH should be those around to 114 ppm (2.5 carbons), and the meta carbon around to 128 ppm (2.4 carbons). The expected contributions of CH signals should be 4 per mol of Bisphenol A moiety. Probably the cross-polarization contact time of 4.5 ms was not enough [69] on the contrary of the two methyl of bridge, that could be assigned to the 42.2 ppm and 32.2 ppm whose correspond to 1 carbon, respectively.

The addition of amine through the aminolysis opening of cyclic carbonate can result in the primary hydroxyl groups (denoted A) and another secondary hydroxyl group (denoted B) containing derivatives. This reaction is chemoselective, prevailing the A derivative [33,77,81]. However, the solid state CPMS spectra were not enough resolved to distinguish the signal of methine of primary alcohol (CH–CH_2OH) and the secondary one (CH–OH). Probably they are overlapped with Ph-O-CH_2 at 69.1 ppm of NIPU-M1 spectrum (6 carbons) or 70.3 ppm of NIPU:Ms1 spectrum (5 carbons). Nevertheless, the signal at 62.7 ppm for NIPU:M1 (0.5 carbon) and 64.2 ppm for NIPU-Ms1 (1 carbon) can be tentatively assigned to CHCH$_2$OH methylene [81].

3.10. Wettability

To infer about the water wettability of the hybrids, static water contact angles have been measured as a function of time. Composite and hybrid materials such as the one presented in this work are not atomically flat and nanometer scale chemically homogeneous, thus the wettability is related to the apparent contact angle (APCA) which is defined as an equilibrium contact angle measured macroscopically [76]. The time behavior of the APCA for the NIPU:M1 (upper left and lower center in Fig. S10) display very similar exponential decay behaviors with time constant of 1.53 ± 0.150 and 2.55 ± 0.214 for the upper left and lower center region in the photo at Fig. S10, respectively. The final APCA for these two NIPU:M1 regions are 63° and 66°, respectively. The upper right graph in Fig. S10 shows the time dependence for the NIPU:M1 region, i.e., for the shattered region as shown in the figure next to the graph. The time dependence in this region is remarkably different from the other ones showing a stepwise behavior. Such behavior indicates a metastable state for water on top of this shattered surface.

The NIPU:Ms1 and NIPU:Ms2 hybrids showed a more regular pattern imaging due to the more regular morphology. The time dependent behavior of these hybrids can be observed in Fig. S11. NIPU:Ms1 showed a linear decrease on APCA while NIPU:Ms2 follows an exponential decay as observed for NIPU:M1 region with time constant 56.2 ± 6.81. The APCA values for NIPU:Ms1 and NIPU:Ms2 are 95.7° and 83.1°, respectively.

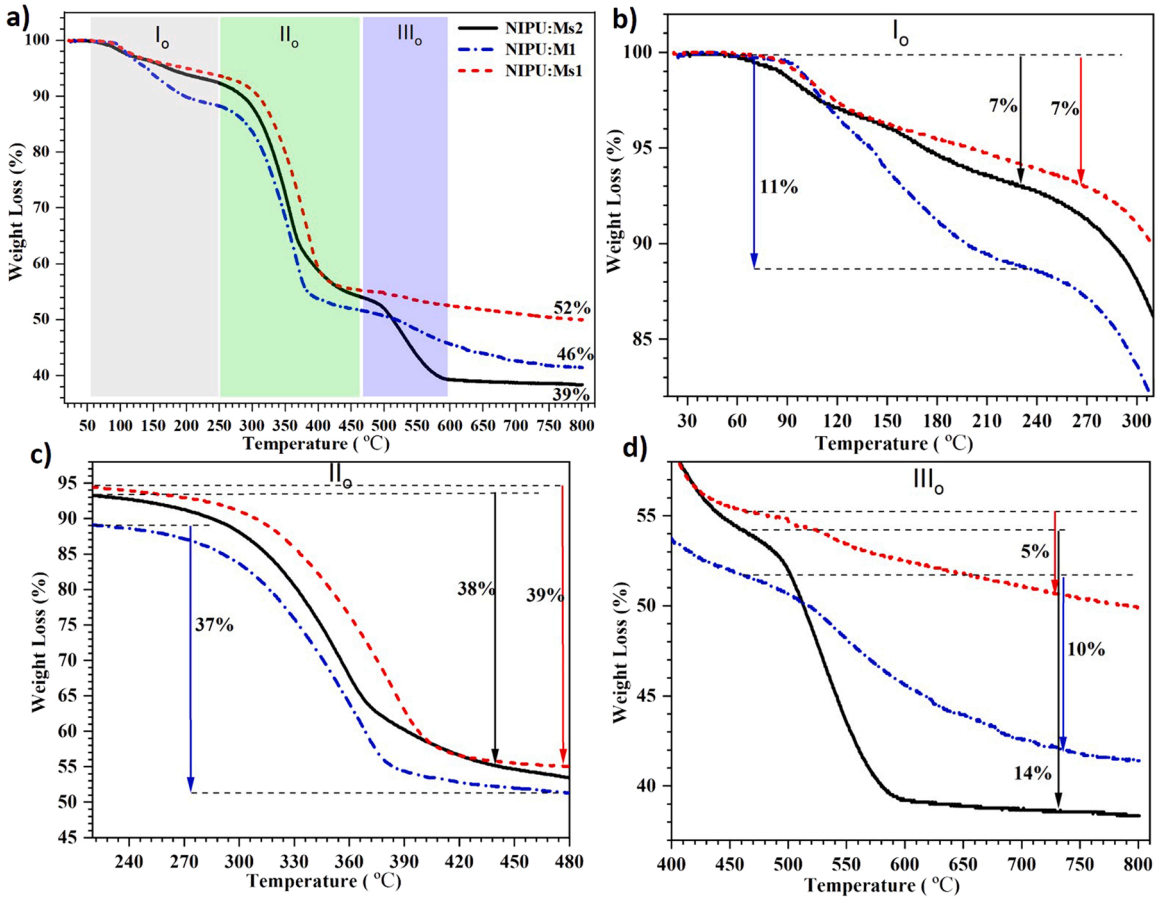

Fig. 6. TGA analysis under inert atmosphere showing the mass loss of hybrids. a) First step degradation from 55 to 250 °C. b) Second degradation step from 250 to 470 °C. c) Third degradation step from 470 to 600 °C.

3.11. Thermal characterization

The thermal stability and pathways degradation of the NIPU materials were evaluated using thermogravimetry in N_2 and dry air dynamic atmospheres. The resulting curves are presented in Fig. 6 and Fig. S12, respectively. Fig. 6-a depicts the TGA curves under N_2 while its first derivative highlighting the decomposition temperatures corresponding to the different mass losses are presented in Fig. 7.

TGA curves under inert atmosphere (Fig. 6-a) revealed a multistage decomposition process with consecutive mass loss steps. In Fig. 6-b, an initial degradation is observed starting at onset 55 ºC for all hybrids, suggesting that all present similar thermal stability.

A first mass loss involving 11% mass loss for the hybrid with non-silylated muscovite (NIPU:M1) and 7% for hybrids with silylated muscovite (NIPU:Ms1 and Ms2) was observed. According to Mourougou-Candoni e Thibaudau [82], flat freshly cleaved mica surfaces are hydrophilic, therefore may be an explanation for the higher mass loss of NIPU:M1 at the first decomposition stage, being assigned to loss of trapped water in the non-silylated mica. The loss of volatiles in NIPU:Ms1 and NIPU:Ms2 may be relative to heteropolycondesation of alkoxy (RO-Si), silanol (HO-Si) of the aminopropyltrimethoxysilane (APTES) silylating agent of the silylated mica, homopolycondesation of alkoxysilane forming multilayers or water absorbed on amino groups of the APTES. The adsorption of APTES on muscovite has been studied by Gölander and Kiss [67,83] revealing the formation of partially hydrolyzed alkoxysilanes as well as by Mourougou-Candoni et al. revealing the formation of multi-layer adsorption [82].

The DTG curves at Fig. 7 show small peaks at the first thermal event (I_0) around 95 and 147 °C for all samples, although their relative intensities are not the same. The NIPU:M1 has very small peak at 147 °C, while the other samples have relatively more intense ones. The two-step thermal event process for I_0 thermal event was confirmed through the derivative curves (DTG) in Fig. 7, hence in agreement with our hypothesis. Thus, the first temperature is likely to be water/solvent entrapped into the material, while the higher temperature can be tentatively assigned to water/ethanol release from the condensation of the Si-OH or Al-OH on muscovite surface with the residual Si-OH and Si-OEt groups of the APTES silylated mica or even homopolycondesation between APTES forming bilayers on mica.

The second thermal event (II_0) has the largest mass loss for all hybrid material as can be seen in Fig. 6-c ranging from 230 to 470 °C. This event can be tentatively assigned to retropolymerization followed by amine and CO_2 release based on the traditional PU thermogravimetric studies [84,85]. Amine release as a consequence of retropolymerization is supported by the low isophorone diamine boiling point, 247 °C. Farid et al. as well as Besse et al. also reported decomposition of biobased platforms NIPU at similar temperatures [86,87]. As indicated in Fig. 6-c, the CCGEBA:IPDA molar ratio has an impact on this degradation step, showing a slightly smaller stability for the hybrid NIPU:Ms2 than the others, with a 30 °C difference between its minima and the one for NIPU:Ms1. Finally, another process within the same range of temperature is the decomposition of DGEBA as reported by Andraschek et al. [12].

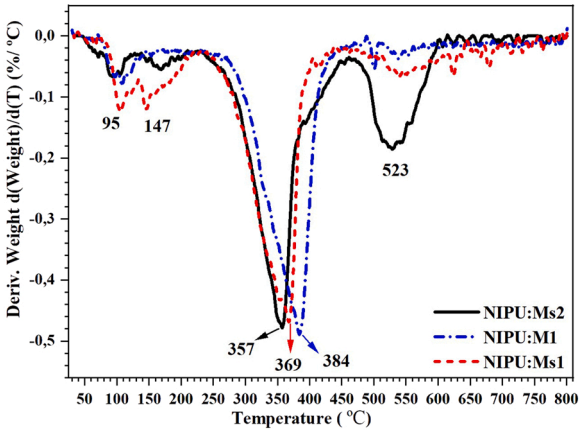

Fig. 7. DTG curve of the NIPU hybrids (inert atmosphere).

The last thermal event (III_0) is more significant for the NIPU:Ms2 than for the other samples (Fig. 6-d). The main difference among NIPU:Ms1 and NIPU:Ms2 is a higher CCGEBA:IPDA molar ratio, this decrease in thermal stability could be assigned to a full decomposition of the organic matter as depicted by Chattopadhyay and Webster [84].

The $Td_{10\%}$ of NIPU:M1 was 198 °C, 309 °C for NIPU:Ms1 and 285 °C for NIPU:Ms2. Moreover, the char yield for all materials is given at 600 ºC in Table 4, thus the hybrids can be classified according their char yield as follows: NIPU:Ms2 < NIPU:M1 < NIPU:Ms1Therefore, higher CCGEBA:IPDA molar ratio results on 14% and 25% lower thermal stability than NIPU:M1 and NIPU:Ms1 hybrids, respectively. Interestingly, for the same molar ratio silylated mica confers 13% higher stability. Thence, CCGEBA in larger amount than the group equivalent is deleterious to the thermal stability of the material.

The thermal behavior under oxidant atmosphere, synthetic air, is shown in TGA curves in Fig. S12-a and DTA curves in Fig. S12-b. It is clear that no decomposition of the muscovite occurs before 480 °C as shown in the insert, implying the thermal events of the hybrids are related to the bisphenol A NIPU itself. The decomposition of all samples started at c.a. 95 °C, suggesting similar thermal stability, in agreement with the results under inert atmosphere. The thermal events are described in Table S5.

3.12. Nanoindentation characterizations

Nanoindentation is now a widely adopted nano-mechanical characterization technique, thus it was applied on the insulating NIPU:Ms1 and NIPU:Ms2 prototypes and, the system DGEBA/IPDA/Silylated mica, as control. Fig. 8 represents a typical loading and unloading curve from indentation experiments.

Curves from Fig. 8 represent the maximum displacement (h_{max}) of the indenter corresponding to the maximum load applied (p_{max}) during the indentation. The nature of the unloading curve is governed by elastic properties of the material and provides information regarding the elastic, viscoelastic and plastic behavior [88]. According to Oliver and Pharr [63], the behavior of both prototypes is typical of an elastoplastic material.

Table 4
Thermal data of NIPU samples under N_2.

Samples	Thermal Event	TGA Temperature Range (°C)	$T_{d10\%}$ (°C)	DTG Peak (°C)	Mass loss (%)	Char yield# (w%)
NIPU:M1	I_0	57–250	198	96 and145	11	–
NIPU:Ms1		56–264	309	108	7	–
NIPU:Ms2		55–233	285	96 and 145	7	–
NIPU:M1	II_0	250–470	–	384	37	–
NIPU:Ms1		240–438	–	369	38	–
NIPU:Ms2		232–462	–	357	39	–
NIPU:M1	III_0	473–734	–	538	10	45.6
NIPU:Ms1		475–615	–	541	5	52.4
NIPU:Ms2		468–604	–	523	14	39.2

At 600 ºC.

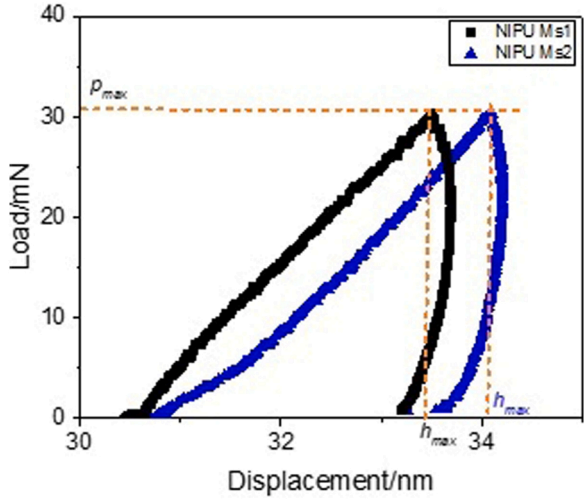

Fig. 8. Indentation load as a function of displacement for NIPU:Ms1 and NIPU:Ms2.

The maximum penetration depth h_{max} at higher load was observed for the prototypes containing silylated mica between 33 nm and 34 nm. Regarding the mechanical properties, such as hardness and elastic modulus, was found for the system NIPU:Ms2 the highest hardness value, 0.41 GPa. When the molar ratio CCGEBA:IPDA was 1:1, the hardness dropped 68% probably due to the smaller crosslinking degree generating a softer surface. The elastic modulus for the prototypes NIPU:Ms1 and NIPU:Ms2 were 2.75 GPa and 5.04 GPa, respectively. The elastic component provided by the urethane linkage on those samples contributed to a low elastic modulus.

3.13. Dielectric response

Values of the dielectric breakdown voltage measured for the hybrid NIPUs are shown in Table 5. These reveal consistent with values expected for mica-based compounds, sizing normally towards the 20–200 kV.mm^{-1} range [88]. Moreover, the real part of capacitance estimated from the impedance data measured in these materials, towards the explored 0.1–100 kHz frequency region, showed values in the 10^{-11} - 10^{-12} F magnitude order, which is typical of bulk (i.e, volume instead of interface) polarization response. For an appropriate comparison between samples, Table 5 includes a summary of the measured data in terms of dielectric constant (ε). A decrease trend of this intrinsic property is observed with increasing frequency, reproducing well the dispersion scenario usually found in materials [89,90]. This is because some polarizable units are supposed to become frozen-like when facing the high speed of the applied alternating electric field. From 1 kHz to above, the changes revealed indeed relatively unimportant, making much realistic comparison between the materials. At 1 kHz, for instance, the dielectric constant values were 8.5, 10.4 and 17.9 for the NIPU:M1, NIPU:Ms1 and NIPU:Ms2, respectively. The lower value of $\varepsilon = 8.5$ processed for NIPU:M1 is coherent with the range of values normally found for mica samples: $\varepsilon \cong 5$–9 [91,92]. Microscopic features related to phases distribution along the silylated mica component, as for NIPU:Ms1 and NIPU:Ms2, is to be here considered as responsible for an enhancement in dielectric constant. The same trend applied when CCGEBA was increased in the formulation, as verified for NIPU:Ms2 (when compared, for instance, to NIPU:Ms1). The dissipation factors, at identical conditions of frequency (1 kHz) and temperature (25 °C), were 0.28, 0.12 and 0.47 for the NIPU:M1, NIPU:Ms1 and NIPU:Ms2, respectively (Table 5). While the best result, say lower dissipation value, was found for NIPU:Ms1, adding CCGEBA excess appears to have a deleterious effect, as measured for NIPU:Ms2. This is in line with the lower dielectric breakdown voltage finally observed for this material, which, according to water absorption, gel content and solvent swelling tests, reveals a higher porous nature. In other words, this material shows a relatively higher propensity to absorb water molecules (including from moisture), expected to traduce into an increase in free space-charge carriers contributing to direct current conductivity and, hence, modulating the overall dissipation factor.

Table 5
Values of dielectric strength and dielectric constant measured for the hybrid NIPUs at room temperature (25 °C).

Material	Dielectric strength (kV.mm^{-1})	Dielectric constant (ε)			
		0,1 kHz	1 kHz	10 kHz	100 kHz
NIPU:M1	19,0	13.0	8.5	6.9	6.0
NIPU: Ms1	20,2	12.5	10.4	9.2	8.4
NIPU: Ms2	16,5	31.4	17.9	12.6	10.2

4. Conclusions

New hybrid Bisphenol A hydroxyurethane-silylated mica powder for insulation applications were prepared in this work, presenting dielectric strength of 20.2 kV/mm and dielectric constant around 10.4 (1 kHz), that qualify this material as a potential candidate for insulating usage, where the mechanical request is inferior. Infrared and ^{13}C MAS NMR proof the formation of the hydroxyurethane, as well as ^{29}Si MAS NMR was paramount on demonstrating the preserved structure of the muscovite inside the Bisphenol A hydroxyurethane-mica powder hybrid. An equimolar ratio between isophorone diamine and bis-cyclocarbonate of bisphenol A presented the best performance according to swelling index, gel content, water absorption, nanoindentation and thermal stability. Thus, it has been demonstrated the preparation of non-toxic hybrid materials by CO_2 fixation and non-isocyanate hydroxyurethane for replacing epoxy-mica paper hybrid system as insulating material.

CRediT authorship contribution statement

Juliana J. Santos: Was responsible for Data curation, Visualization, Writing – original draft, Writing – review & editing. **José H. Lopes**: Was responsible for Conceptualization, Methodology, Data curation, Investigation, Visualization, Writing – original draft. **Mateus B. Simões**: For Conceptualization, Methodology, Investigation. **Kelen M.F. Rossi de Aguiar, Jean-Claude MPeko, Renato G. Jasinevicius, Eder T. Cavalheiro, Hidetake Imasato**: Were responsible for Data curation, Writing – original draft, Writing – review & editing. **Ubirajara P. Rodrigues-Filho**: Was responsible for Conceptualization, Data curation, Formal analysis, Funding acquisition, Project administration, Resources, Visualization, Writing – original draft, Writing – review & editing.

Declaration of Competing Interest

The authors declare that they have no known competing financial interests or personal relationships that could have appeared to influence the work reported in this paper.

Data availability

Data will be made available on request.

Acknowledgments

The solid-state NMR experiments were kindly provided by Luiz Alberto Colnago and Viviane Faria Soares from Embrapa Instrumentaç ão, São Carlos, SP, Brazil. This research has been funded by Fundação de Amparo à Pesquisa do Estado de São Paulo (FAPESP),

Brazil, Program “Pesquisa sobre Mudanças Climáticas Globais / PFPMCG”, grant # 2018/19785–12018/19785-1.

Appendix A. Supporting information

Supplementary data associated with this article can be found in the online version at doi:10.1016/j.jcou.2022.102303.

References

[1] H. Li, et al., Dielectric properties of graphene-filled epoxy nanocomposite with enhanced thermal conductivity, Int. Symp. . Electr. Insul. Mater. (ISEIM) (2017) 149–152, https://doi.org/10.23919/ISEIM.2017.8088699.

[2] A. Rybak, J. Nieroda, Aluminosilicate-epoxy resin composite as novel material for electrical insulation with enhanced mechanical properties and improved thermal conductivity, Polym. Compos. 40 (2019) 3182–3188, https://doi.org/10.1002/pc.25167.

[3] B. Nageshwar Rao, J. Sundara Rajan, B. Ramachandra, Application of RVM technique to study the polarization and De-polarization characteristics associated with thermal ageing of Epoxy-Mica composite, *2012 IEEE 10th Int. Conf. Prop. Appl. Dielectr. Mater. (ICPDAM)*; Bangalore (2012) 3–6.

[4] T. Tanase, T. Kato, S. Tanaka, A. Sano, H. Kojima, K. Fukushima, Y. Takezawa, Prolonging electrical lifetime of mesogenic epoxy based alumina-mica composite sheet: optimization of mica content by electrical tree progress simulation, IEEE Trans. Dielectr. Electr. Insul. 25 (2018) 2212–2219.

[5] R. Vogelsang, T. Farr, K. Frohlich, The effect of barriers on electrical tree propagation in composite insulation materials, IEEE Trans. Dielectr. Electr. Insul. 13 (2006) 373–382, https://doi.org/10.1109/TDEI.2006.1624282.

[6] B. Ellis, in: B. Ellis (Ed.), Introduction to the Chemistry, Synthesis, Manufacture and Characterization of Epoxy Resins, Chemistry and Technology of Epoxy Resins. Springer, Dordrecht, 1993, pp. 1–36, https://doi.org/10.1007/978-94-011-2932-9_1.

[7] T. Heid, M. Fréchette, E. David, Epoxy/BN micro- and submicro-composites: dielectric and thermal properties of enhanced materials for high voltage insulation systems, IEEE Trans. Dielectr. Electr. Insul. 22 (2015) 1176–1185, https://doi.org/10.1109/TDEI.2015.7076820.

[8] G. Tesoro, Epoxy resins-chemistry and technology, in: Clayton A. May (Ed.), 2nd edition.,J. Polym. Sci. C Polym. Lett., 26, Marcel Dekker, New York, 1988, https://doi.org/10.1002/pol.1988.140261212.

[9] I.A. Tsekmes, R. Kochetov, P.H.F. Morshuis, J.J. Smit, Thermal conductivity of polymeric composites: a review, *2013 IEEE Int. Conf. Solid Dielectr.*, Bologna (2013) 678–681, https://doi.org/10.1109/ICSD.2013.6619698.

[10] K. Tanaka, H. Kojima, M. Onoda, K. Suzuki, Prediction of residual breakdown electrical field strength of epoxy-mica paper insulation systems for the stator winding of large generators, IEEE Trans. Dielectr. Electr. Insul. 22 (2015) 1118–1123, https://doi.org/10.1109/TDEI.2015.7076813.

[11] F. Liebau, Structural Chemistry of Silicates: Structure, Bonding, and Classification, Springer-Verlag,, Berlin, Heidelberg and New York, 1985, p. 1985.

[12] N. Andraschek, A.J. Wanner, C. Ebner, G. Riess, Mica/Epoxy-Composites in the Electrical Industry: Applications, Composites for Insulation, and Investigations on Failure Mechanisms for Prospective Optimizations, Polymers 8 (2016) 201, https://doi.org/10.3390/polym8050201.

[13] Andres, W.H.; Mica paper insulations for conductors and cables, in EIC 13th Electrical/Electronics Insulation Conference, 1977, p. 225–230, DOI: 10.1109/EIC.1977.7461952.

[14] M.A. Chaudhry, A.K. Jonscher, The dielectric properties of mica paper in variable temperature and humidity, J. Mater. Sci. 20 (1985) 3581–3589, https://doi.org/10.1007/BF01113764.

[15] Reid, R.T.; Nikrandt, M.D.; Dolence, D.; Scherer, D.N. Electrical machine coil insulation system and method, 2013, US20130221790A1, United States.

[16] L. Virsberg, A. Björklund, New type of turn insulation for medium-sized, high-voltage electrical machines, EIC 13th Electr. /Electron. Insul. Conf. (1977) 199–201, https://doi.org/10.1109/EIC.1977.7461946.

[17] K.A. Andrianov, M.B. Fromberg, K.I. Zabyrina, L.I. Sorokina, Graft copolymers from polyorganosiloxanes and epoxide resins, *Polym. Sci.* U. S. S. R. 3 (6) (1962), 10741080, https://doi.org/10.1016/0032-3950(62)90013-8.

[18] S. Sprenger, Epoxy resins modified with elastomers and surface-modified silica nanoparticles, Polymer 54 (18) (2013) 4790–4797, https://doi.org/10.1016/j.polymer.2013.06.011.

[19] B.G. Soares, B.M. Bezerra, D.N. Barros, A.A. Silva, Epoxy modified with urea-based ORMOSIL and isocyanate-functionalized polybutadiene: Viscoelastic and adhesion properties, Compos. Part B Eng. 168 (2019) 334–341, https://doi.org/10.1016/j.compositesb.2019.03.058.

[20] A. Sienkiewicz, P. Czub, Blocked isocyanates as alternative curing agents for epoxy-polyurethane resins based on modified vegetable oils, *Express Polym. Lett.* 13 (2019) 642–655, https://doi.org/10.3144/expresspolymlett.2019.54.

[21] A.R. Morales, Morfologia e propriedades dinâmicas e mecânicas de resina epóxi/elastômero reativo, Master's Dissertation, Universidade Federal de São Carlos,, Brazil, 1989.

[22] M. Martina, D.W. Hutmacher, Biodegradable polymers applied in tissue engineering research: a review, *Polym. Int.* 56 (2007) 145–157, https://doi.org/10.1002/pi.2108.

[23] E. Sharmin, F. Zafar, Polyurethane: An Introduction, Polyurethane, IntechOpen,, 2012, pp. 3–15, https://doi.org/10.5772/51663.

[24] A. Cornille, R. Auvergne, O. Figovsky, B. Boutevin, S. Caillol, A perspective approach to sustainable routes for non-isocyanate polyurethanes, Eur. Polym. J. 87 (2017) 535–552, https://doi.org/10.1016/j.eurpolymj.2016.11.027.

[25] J.O. Akindoyo, M.D.H. Beg, S. Ghazali, M.R. Islam, N. Jeyaratnam, A.R. Yuvaraj, Polyurethane types, synthesis and applications – a review, RSC Adv. 6 (2016) 114453–114482, https://doi.org/10.1039/C6RA14525F.

[26] D. Randall, S. Lee, The Polyurethanes Book, Huntsman Polyurethanes; Distributed by John Wiley & Sons,, Everberg Belgium New York, 2002, pp. 9–22.

[27] J. He, J.J. Li, Y. Wen, H.W. Tai, Y. Yu, W.C. Qin, L.M. Su, Y.H. Zhao, Investigation on modes of toxic action to rats based on aliphatic and aromatic compounds and comparison with fish toxicity based on exposure routes, Chemosphere 128 (2015) 111–117, https://doi.org/10.1016/j.chemosphere.2015.01.028.

[28] D. Bello, C.A. Herrick, T.J. Smith, S.R. Woskie, R.P. Streicher, M.R. Cullen, Y. Liu, C.A. Redlich, Skin exposure to isocyanates: reasons for concern, Environ. Health Perspect. 115 (2007) 328–335, https://doi.org/10.1289/ehp.9557.

[29] O. Figovsky, A. Leykin, L. Shapovalov, Non-isocyanate polyurethanes – yesterday, today and tomorrow, Altern. Energy Ecol. 3–4 (2016) 95–108, https://doi.org/10.15518/isjaee.2016.03-04.009.

[30] J. Guan, Y. Song, Y. Lin, X. Yin, M. Zuo, Y. Zhao, X. Tao, Q. Zheng, Progress in study of non-isocyanate polyurethane, Ind. Eng. Chem. Res. 50 (2011) 6517–6527.

[31] M.S. Kathalewar, P.B. Joshi, A.S. Sabnis, V.C. Malshe, Non-isocyanate polyurethanes: from chemistry to applications, RSC Adv. 3 (2013) 4110–4129, https://doi.org/10.1039/C2RA21938G.

[32] Groszos, S.J.; Drechsel, E.K.; Method of preparing a polyurethane, 1957; US2802022A, United States.

[33] F. Günther, M. Batista Simões, H. Imasato, U. Pereira Rodrigues-Filho, Experimental and Theoretical assessment of the Aminolysis of Cyclo Carbonate to form polyhydroxyurethanes, Mater. Today Commun. 21 (2019), 100604, https://doi.org/10.1016/j.mtcomm.2019.100604.

[34] F. Camara, S. Benyahya, V. Besse, G. Boutevin, R. Auvergne, B. Boutevin, S. Caillol, Reactivity of secondary amines for the synthesis of non-isocyanate polyurethanes, Eur. Polym. J. 55 (2014) 17–26, https://doi.org/10.1016/j.eurpolymj.2014.03.011.

[35] M.V. Zabalov, R.P. Tiger, A.A. Berlin, Mechanism of urethane formation from cyclocarbonates and amines: a quantum chemical study, Russ. Chem. Bull. 61 (2012) 518–527, https://doi.org/10.1007/s11172-012-0076-8.

[36] O. Figovsky, L. Shapovalov, A. Leykin, O. Birukova, R. Potashnikova, Progress in Elaboration of Nonisocyanate Polyurethanes Based on Cyclic Carbonates, Int. Lett. Chem. Phys. Astron. 3 (2013) 52–66, https://doi.org/10.18052/www.scipress.com/ILCPA.3.52.

[37] O. Figovsky, D. Beilin, Advanced Polymer Concretes and Compounds, CRC Press, Inc.,, Boca Raton, USA, 2013, https://doi.org/10.1201/b16237.

[38] H. Liang, Q. Gao, Synthesis and properties of Non-isocyanate polyurethane Based on Aromatic amine, IOP Conf. Ser.: Mater. Sci. Eng. 612 (2019), 022030, https://doi.org/10.1088/1757-899X/612/2/022030.

[39] M. Ghasemlou, F. Daver, E.P. Ivanova, B. Adhikari, Synthesis of green hybrid materials using starch and non-isocyanate polyurethanes, Carbohydr. Polym. 229 (2020), 115535, https://doi.org/10.1016/j.carbpol.2019.115535.

[40] R.H. Lambeth, A. Rizvi, Mechanical and adhesive properties of hybrid epoxypolyhydroxyurethane network, Polym. *Polym. (Guildf.).* 183 (2019), 121881.

[41] A. Cornille, J. Serres, G. Michaud, F. Simon, S. Fouquay, B. Boutevin, S. Caillol, Syntheses of epoxyurethane polymers from isocyanate free oligo-polyhydroxyurethane, Eur. Polym. J. 75 (2016) 175–189, https://doi.org/10.1016/j.eurpolymj.2015.12.017.

[42] R. Ghanbaralizadeh, H. Bouhendi, K. Kabiri, M. Vafayan, A novel method for toughening epoxy resin through CO2 fixation reaction, J. CO2 Util. 16 (2016) 225–235.

[43] S. Kranias, C. Bureau, D.P. Chong, I. George, P. Viel, Evidencing intermolecular effects with core-level photoelectron spectroscopy via the accurate density functional calculation of core-electron binding energies on model systems: γ-APS as a test, J. Phys. Chem. B 101 (1997) 10254–10261, https://doi.org/10.1021/jp971996b.

[44] J.S. Andresa, R.M. Reis, E.P. Gonzalez, L.S. Santos, M.N. Eberlin, P.A.D. P. Nascente, S.T. Tanimoto, S.A.S. Machado, U.P. Rodrigues-Filho, Adsorption of silanes bearing nitrogenated Lewis bases on SiO2/Si (100) model surfaces, J. Colloid Interface Sci. 286 (2005) 303–309, https://doi.org/10.1016/j.jcis.2005.01.019.

[45] H. Barthel, M. Heinemann, F. Hermann, A. Altenbuchner, Process for Sylylation of Inorganic Oxides, European Patent Office, 1997. EP0686676A1.

[46] G. Stephen Caravajal, D.E. Leyden, G.R. Quinting, G.E. Maciel, Structural characterization of (3-aminopropyl)triethoxysilane-modified silicas by silicon-29 and carbon-13 nuclear magnetic resonance, Anal. Chem. 60 (1988) 1776–1786, https://doi.org/10.1021/ac00168a027.

[47] B.T. Liu, J.R. Syu, D.H. Wang, Conductive polyurethane composites containing polyaniline-coated nano-silica, J. Colloid Interface Sci. 393 (2013) 138–142, https://doi.org/10.1016/j.jcis.2012.11.028.

[48] I.K. Tonle, E. Ngameni, A. Walcarius, From clay-to organoclay-film modified electrodes: tuning charge selectivity in ion exchange voltammetry, Electrochim. Acta 49 (2004) 3435–3443, https://doi.org/10.1016/j.electacta.2004.03.012.

[49] S.M. Cakić, M.D. Valcic, I.S. Ristić, T. Radusin, M.J. Cvetinov, J. Budinski-Simendić, Waterborne polyurethane-silica nanocomposite adhesives based on castor oil-recycled polyols: Effects of (3-aminopropyl)triethoxysilane (APTES)

content on properties, Int. J. Adhes. Adhes. 90 (2019) 22–31, https://doi.org/10.1016/j.ijadhadh.2019.01.005.
[50] S. Jia, Z. Wang, Y. Zhu, L. Chen, L. Fu, Composites of poly(lactic) acid/thermoplastic polyurethane/mica with compatibilizer: morphology, miscibility and interphase, RSC Adv. 5 (2015) 98915–98924, https://doi.org/10.1039/C5RA17938F.
[51] C. Fernández-dacosta, V. Stojcheva, A. Ramirez, Closing carbon cycles: Evaluating the performance of multi-product CO2 utilisation and storage configurations in a refinery, J. CO2 Util. 23 (2018) 128–142, https://doi.org/10.1016/j.jcou.2017.11.008.
[52] J. Rockström, H.J. Schellnhuber, B. Hoskins, V. Ramanathan, P. Schlosser, G. P. Brasseur, O. Gaffney, C. Nobre, M. Meinshausen, J. Rogelj, W. Lucht, The world's biggest gamble, Earth's Futur 4 (2016) 465–470, https://doi.org/10.1002/2016EF000392.
[53] Aresta, M.; Carbon Dioxide as Chemical Feedstock; Aresta, M., Org.; 1st ed; Wiley-VCH Verlag GmbH & Co. KGaA: Berlin, 2010.
[54] F.D. Meylan, V. Moreau, S. Erkman, CO2 utilization in the perspective of industrial ecology, an overview, J. CO2 Util. 12 (2015) 101–108, https://doi.org/10.1016/j.jcou.2015.05.003.
[55] V. Duraccio, M.G. Gnoni, V. Elia, Carbon Capture and Reuse in an Industrial District: A Technical and Economic Feasibility Study, J. CO2 Util. 10 (2015) 23–29, https://doi.org/10.1016/j.jcou.2015.02.004.
[56] Global Mica Paper Market 2019 With Top Countries Data: Market Size, Concentration Rate, Production Volume, Price, Gross Margin and Revenue ⟨https://www.theexpresswire.com/pressrelease/Global-Mica-Paper-Market-2019-With-Top-Countries-Data-Market-Size-Concentration-Rate-Production-Volume-Price-Gross-Margin-and-Revenue_10462209⟩.
[57] K.L. Mittal, Silanes and Other Coupling Agents, CRC Press,, Boca Raton, 2009.
[58] X. Ge, Y. Zhang, F. Deng, U.R. Cho, Effects of silane coupling agents on tribological properties of bentonite/nitrile butadiene rubber composites, Polym. Compos. 38 (2017) 2347–2357, https://doi.org/10.1002/pc.23817.
[59] International Organization for Standardization, 1999, Plastics — Epoxy compounds — Determination of epoxy equivalent (ISO 3001:1999).
[60] ASTM International; Standard Test Method for Water Absorption of Plastics. ASTM Stand. 2018, 4.
[61] ASTM D149-20, Standard Test Method for Dielectric Breakdown Voltage and Dielectric Strength of Solid Electrical Insulating Materials Under Direct-Voltage. Astm, 2020, pp. 1–6.
[62] R.Y. Yee, T.S. Stephens, A TGA technique for determining graphite fiber content in epoxy composites, Thermochim. Acta 272 (1996) 191–199, https://doi.org/10.1016/0040-6031(95)02606-1.
[63] W.C. Oliver, G.M. Pharr, Measurement of hardness and elastic modulus by instrumented indentation: Advances in understanding and refinements to methodology, J. Mater. Res. 19 (2004) 3, https://doi.org/10.1557/jmr.2004.19.1.3.
[64] E.S. Gadelmawla, M.M. Koura, T.M.A. Maksoud, I.M. Elewa, H.H. Soliman, Roughness parameters, J. Mater. Process. Technol. 123 (2002) 133–145, https://doi.org/10.1016/S0924-0136(02)00060-2.
[65] V.V. Alekseev, S.V. Vladimirov, L.I. Maklakov, V.L. Furer, A.L. Furer, Vibrational spectra of some urethanes and the assignment of bands related to urethane group vibrations, J. Appl. Spectrosc. 28 (1978) 711–716, https://doi.org/10.1007/BF00609779.
[66] C.G. Gölander, E. Kiss, Surface grafting of polyethyleneoxide optimized by means of ESCA, Progr. Colloid Polym. Sci. 74 (1987) 113, https://doi.org/10.1007/BF01191021.
[67] H.C. Marsmann, 29Si NMR studies on silicate solutions in water, Z. für Naturforsch. B 29 (7–8) (1974) 495–499, https://doi.org/10.1515/znb-1974-7-810.
[68] W. Kolodziejski, J. Klinowski, Kinetics of cross-polarization in solid-state NMR: a guide for chemists, Chem. Rev. 102 (2002) 613–628, https://doi.org/10.1021/cr000060n.
[69] G.E. Maciel, D.W. Sindorf, Silicon-29 Nuclear Magnetic Resonance Study of the Surface of Silica Gel by Cross Polarization and Magic-Angle Spinning, J. Am. Chem. Soc. 102 (1980) 7606–7607.
[70] M.R. Johnston, J.R. Gascooke, A.V. Ellis, S.C. Leterme, Diatoms response to salinity changes: investigations using single pulse and cross polarisation magic angle spinning ^{29}Si NMR spectra, Analyst 143 (2018) 4930–4935, https://doi.org/10.1039/C8AN00948A.
[71] W.F. Bleam, Soil and Environmental Chemistry, Academic Press, Inc,, Burlington, 2012, pp. 85–116.
[72] E. Lippmaa, M. Magi, A. Samoson, G. Engelhard, A.R. Grimmer, Structural studies of silicates by solid-state high-resolution silicon-29 NMR, J. Am. Chem. Soc. 102 (1980) 4889–4893, https://doi.org/10.1021/ja00535a008.
[73] E. Lippmaa, M. Mági, A. Samoson, M. Tarmak, G. Engelhardt, Investigation of the structure of zeolites by solid-state high-resolution silicon-29 NMR spectroscopy, J. Am. Chem. Soc. 103 (1981) 4992–4996, https://doi.org/10.1021/ja00407a002.
[74] J. Sanz, J. Serratosa, Silicon-29 and aluminum-27 high-resolution MAS-NMR spectra of phyllosilicates, J. Am. Chem. Soc. 106 (1984) 4790–4793, https://doi.org/10.1021/ja00329a024.
[75] C.A. Weiss Jr, S.P. Altaner, R.J. Kirkpatrick, High-resolution ^{29} Si NMR spectroscopy of 2:1 layer silicates; correlations among chemical shift, structural distortions, and chemical variations. Am. Mineral. 72 (1987) 935–942.
[76] B. Ochiai, S. Inoue, T. Endo, One-pot non-isocyanate synthesis of polyurethanes from bisepoxide, carbon dioxide, and diamine, J. Polym. Sci. Part A Polym. Chem. 43 (2005) 6613–6618, https://doi.org/10.1002/pola.21103.
[77] X. Wu, S.T. Burns, K.W. Zilm, Spectral Editing in CPMAS NMR. Generating Subspectra Based on Proton Multiplicities, J. Magn. Reson. Ser. A 111 (1994) 29–36, https://doi.org/10.1006/jmra.1994.1222.
[78] P.G. Hatcher, Chemical structural studies of natural lignin by dipolar dephasing solid-state 13C nuclear magnetic resonance, Org. Geochem. 11 (1987) 31–39, https://doi.org/10.1016/0146-6380(87)90049-0.
[79] R.K. Harris, A.M. Kenwright, K.J. Packer, Non-Quaternary Suppression with Flip-Back: a Useful Technique for High-Resolution NMR of Solids, Magn. Reson. Chem. 23 (1985) 216–217, https://doi.org/10.1002/mrc.1260230318.
[80] H. Tomita, F. Sanda, T. Endo, Model reaction for the synthesis of polyhydroxyurethanes from cyclic carbonates with amines: Substituent effect on the reactivity and selectivity of ring-opening direction in the reaction of five-membered cyclic carbonates with amine, J. Polym. Sci. A Polym. Chem. 39 (2001) 3678–3685, https://doi.org/10.1002/pola.10009.
[81] N. Mourougou-Candoni, F. Thibaudau, Formation of aminosilane film on mica, J. Phys. Chem. B. 113 (2009) 13026–13034, https://doi.org/10.1021/jp903021e.
[82] E. Kiss, C.G. Gölander, Chemical derivatization of muscovite mica surfaces, Colloids Surf. 49 (1990) 335–342, https://doi.org/10.1016/0166-6622(90)80114-J.
[83] D.K. Chattopadhyay, D.C. Webster, Thermal stability and flame retardancy of polyurethanes, Prog. Polym. Sci. *Prog. Polym. Sci.,* 34 (2009) 1068–1133, https://doi.org/10.1016/j.progpolymsci.2009.06.002.
[84] C.G. Mothé, C.R. de Araujo, Thermal and mechanical caracterization of polyuretane composites with Curaua fibers, Polímeros 14 (4) (2004) 274–278, https://doi.org/10.1590/S0104-14282004000400014.
[85] M.E. Farid, M.A. El-Sockary, A.M. El-Saeed, A.I. Hashem, O.M. Abo Elenien, M. S. Selim, S.E. Park, An eco-friendly non-isocyanate polyurethane treated by CO_2 as flame retardant nanocomposite coating/ZrO_2@SiO_2. Mater. Res. Express (2019) 6, https://doi.org/10.1088/2053-1591/ab0da3.
[86] V. Besse, R. Auvergne, S. Carlotti, G. Boutevin, B. Otazaghine, S. Caillol, J.-P. Pascault, B. Boutevin, Synthesis of isosorbide based polyurethanes: An isocyanate free method, React. Funct. Polym. 73 (2013) 588–594, https://doi.org/10.1016/j.reactfunctpolym.2013.01.002.
[87] T. Iqbal, B.J. Briscoe, P.F. Luckham, Surface plasticization of poly(ether ether ketone), Eur. Polym. J. 47 (2011) 2244–2258, https://doi.org/10.1016/j.eurpolymj.2011.09.022.
[88] W. Zhao, Y. Xu, C. Song, J. Chen, X. Liu, Polyimide/mica hybrid films with low coefficient of thermal expansion and low dielectric constant, e-Polym. 19 (2019) 181–189, https://doi.org/10.1515/epoly-2019-0019.
[89] M.F. García-Sánchez, J.C. M'Peko, A.R. Ruiz-Salvador, G. Rodríguez-Gattorno, Y. Echevarría, F. Fernández-Gutierrez, A. Delgado, An elementary picture of dielectric spectroscopy in solids: Physical basis, J. Chem. Educ. 80 (2003) 1062–1073, https://doi.org/10.1021/ed080p1062.
[90] S. Okabe, N. Hayakawa, H. Murase, H. Hama, H. Okubo, Common insulating properties in insulating materials, IEEE Trans. Dielectr. Electr. Insul. 13 (2) (2006) 327–335, https://doi.org/10.1109/TDEI.2006.1624277.
[91] M. Jayalakshmi, K. Balasubramanian, Simple capacitors to supercapacitors - an overview, Int. J. Electrochem. Sci. 3 (2008) 1196–1217.
[92] N.A.B. Zulkifli, M.A. Johar, O.M.F. Marwah, M.H.I. Ibrahim, Review on advances of functional material for additive manufacturing, IOP Conf. Ser. Mater. Sci. Eng. (2017) 226, https://doi.org/10.1088/1757-899X/226/1/012177.